Analytica Chimica Acta 909 (2016) 109–120

Contents lists available at ScienceDirect

Analytica Chimica Acta

journal homepage: www.elsevier.com/locate/aca

Molecular structure and thermodynamic predictions to create highly sensitive microRNA biosensors

Nicholas E. Larkey, Corinne N. Brucks, Shan S. Lansing, Sophia D. Le, Natasha M. Smith, Victoria Tran, Lulu Zhang, Sean M. Burrows*

Department of Chemistry, Oregon State University, 153 Gilbert Hall, Corvallis, OR 97331, United States

HIGHLIGHTS

- Challenges facing highly sensitive miRNA biosensor designs are addressed.
- Thermodynamic and molecular structure design metrics for reporter+probe biosensors are proposed.
- The influence of ideal and non-ideal reporter hairpin structures on reporter+probe formation and signal change are discussed.
- 5–9 nM limits of detection were observed with no interference from off-analytes.

GRAPHICAL ABSTRACT

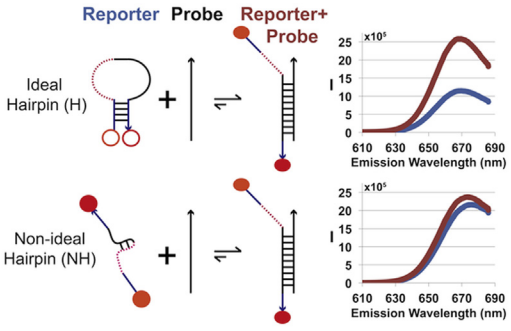

ARTICLE INFO

Article history:
Received 31 August 2015
Received in revised form
24 December 2015
Accepted 30 December 2015
Available online 7 January 2016

Keywords:
Nucleic-acids
Thermodynamics
Hairpin
Displacement
Dimer
Fluorescence

ABSTRACT

Many studies have established microRNAs (miRNAs) as post-transcriptional regulators in a variety of intracellular molecular processes. Abnormal changes in miRNA have been associated with several diseases. However, these changes are sometimes subtle and occur at nanomolar levels or lower. Several biosensing hurdles for *in situ* cellular/tissue analysis of miRNA limit detection of small amounts of miRNA. Of these limitations the most challenging are selectivity and sensor degradation creating high background signals and false signals. Recently we developed a reporter+probe biosensor for let-7a that showed potential to mitigate false signal from sensor degradation. Here we designed reporter+probe biosensors for miR-26a-2-3p and miR-27a-5p to better understand the effect of thermodynamics and molecular structures of the biosensor constituents on the analytical performance. Signal changes from interactions between Cy3 and Cy5 on the reporters were used to understand structural aspects of the reporter designs. Theoretical thermodynamic values, single stranded conformations, hetero- and homodimerization structures, and equilibrium concentrations of the reporters and probes were used to interpret the experimental observations. Studies of the sensitivity and selectivity revealed 5–9 nM detection limits in the presence and absence of interfering off-analyte miRNAs. These studies will aid in determining how to rationally design reporter+probe biosensors to overcome hurdles associated with highly sensitive miRNA biosensing.

1. Introduction

MicroRNAs (miRNAs) are an emerging class of biomarkers that

* Corresponding author.
E-mail address: sean.burrows@oregonstate.edu (S.M. Burrows).

http://dx.doi.org/10.1016/j.aca.2015.12.040
0003-2670/

may aid in understanding, diagnosing, and tracking disease progression. One role of miRNAs in biology is to regulate protein expression by interacting with messenger RNA (mRNA) to disrupt translation. In many diseases, the expression of miRNA is altered leading to changes in protein expression, sometimes resulting in an altered phenotype. *In situ* miRNA analysis is needed to fully understand how miRNA regulate gene expression as miRNA often target different messenger RNA in a cell- and tissue-specific manner [1]. To achieve this goal miRNA biosensors are needed that can detect low levels and small changes in miRNA concentration, particularly in the femtomolar to nanomolar range [2–6].

In general, *in situ* miRNA detection is qualitative or semi-quantitative [1,5,7,8]. Recent reports [9,10] indicate that *in situ* detection of miRNA profiles in cells and tissues as a means for diagnostics and the study of disease progression have been hampered due to insufficient sensitivity, selectivity, and robustness of miRNA biosensors [6]. Standard fluorescence *in situ* hybridization (FISH) techniques have several limitations for low abundance miRNA detection: (1) loss of miRNA from copious rinsing steps, (2) often require secondary sensing with horseradish peroxidase or other enzymatic treatment, (3) long time-to-result, and (4) can only be used on fixed cells and tissues [5,11]. Current biosensors capable of *in situ* nucleic acid analysis, such as molecular beacons or ratiometric bimolecular beacons are limited by intracellular nucleases that often degrade the biosensors, leading to an increase in false signals [12,13].

To overcome the issues relating to false signals, our group recently developed a competitive binding biosensor [14,15]. In the presence of a specific miRNA the biosensor releases a self-complementary reporter capable of Förster Resonance Energy Transfer (FRET). We designed these biosensors for *in situ* analyses [10] with a faster time-to-result than quantitative reverse transcription polymerase chain reaction (RT-qPCR) [16,17], microarrays [18], and FISH [19]. Our sensor, referred to as a 'reporter+probe biosensor', has a partially complementary double-stranded design containing a probe sequence and a reporter sequence with dyes on the 3' (3-prime) and 5' (5-prime) ends. The probe strand is completely complementary to the analyte of interest, and the reporter strand is only partially complementary to the probe to permit competitive binding of the miRNA analyte to the probe. The competitive reaction, referred to by some as a toehold-mediated strand displacement/exchange [20], releases the self-complementary reporter from the probe, allowing the reporter to fold onto itself (Scheme 1). Reporters are designed to form an ideal hairpin structure that brings the 3′ and 5′ ends (containing the reporting dyes) into the FRET distance. However, some reporter designs can form a non-ideal internal hairpin that raises the baseline signal due to increased dye-to-dye distance. Designing these reporter sequences to work in an ideal manner takes into account thermodynamics [21–23], kinetics [24,25], and conformation of the reporter strand.

In our previous work, we developed a reporter+probe biosensor that was selective for let-7a [14,15]. Let-7a is one of the thousands of miRNAs that have been discovered and among those that have been found to regulate disease progression [1,26–31]. Here we investigated multiple reporters to be used in reporter+probe biosensors for two different mouse-derived miRNAs associated with cancer progression: miR-26a-2-3p and miR-27a-5p [32–36]. In this work we will build upon our previous research [14,15] to further examine how the predicted thermodynamic and structural parameters of the reporters, probes, and analytes influence the analytical performance of reporter+probe biosensors. Similar to work by others [24,37,38], the relationship between the Cy3 and Cy5 dye emission was used to understand the conformational states of the reporters in solution with and without probe, and was related to the predicted conformations. Specifically, we will discuss the importance of changes in thermodynamic values, molecular structures, and base pairing before and after reporter+probe formation and subsequent probe+analyte formation. To the best of our knowledge, we were the first group to describe a competitive nucleic acid biosensor that uses a self-complementary reporting molecule to reduce false signals [14,15]. This design has since grown in popularity for use in other technologies like Nanoflares for messenger RNA (commercially known as SmartFlares®) [39] and molecular sentinels [40]. The results of the work presented here will enable the community to rationally design reporter+probe biosensors to achieve a robust, selective, and sensitive biosensor with minimal false signals.

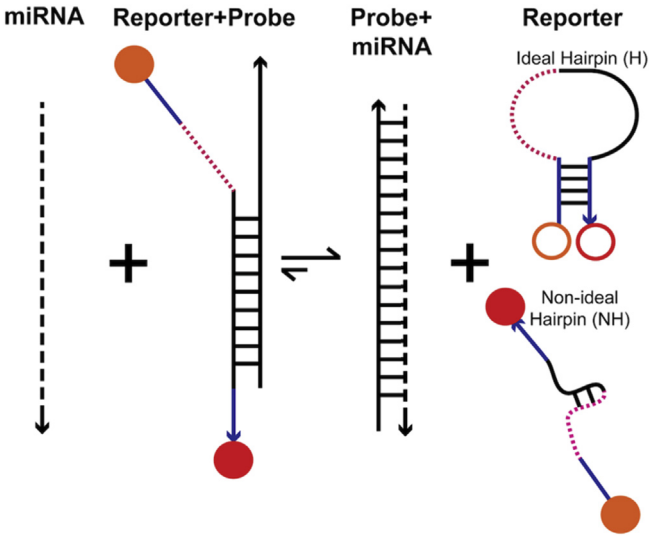

Scheme 1. Response of reporter+probe biosensor to miRNA analyte. The miRNA (down arrow with dashed line) reacts with reporter+probe complex to form the probe+miRNA complex and free reporter. Reporter (Down arrow with solid and dashed regions) is only partially complementary to probe (Up arrow with solid line) in the region indicated in black. The dotted red region of the reporter is not complementary to probe, and the blue region represents the reporters stems. When in the hairpin conformation, the reporter forms a stem-loop that is either ideal with 5′ and 3′ ends directly adjacent to each other, or a non-ideal hairpin that separates the dyes at different distances (Colored circles, orange for Cy3 and red for Cy5). Empty colored circles indicate quenched emission, and filled circles indicate unquenched emission.

2. Experimental

2.1. Reporter design procedure

The process for designing the biosensor sequences is outlined in Scheme 2. DNA analogs of each miRNA strand were used as a substitute because RNA is more susceptible to degradation than DNA. A MATLAB program developed in-house was used to design the nucleic acid sequences for the reporter+probe biosensors based on a particular miRNA analytes, in this case they were miR-26a-2-3p and miR-27a-5p. The computer program starts by designing a probe strand that is fully complementary to a given miRNA analyte. Several reporter strands were then made to be partially complementary to the probe. For consistency each of the reporters in this study contained the same stem sequence, 5′-CGATG——CATCG-3′. The computer program allows control over the length of both the complementary and non-complementary regions on the reporter. The non-complementary regions of the reporters were made of random nucleic acid sequences. The reporters were then filtered to remove those reporters whose non-complementary region bind to

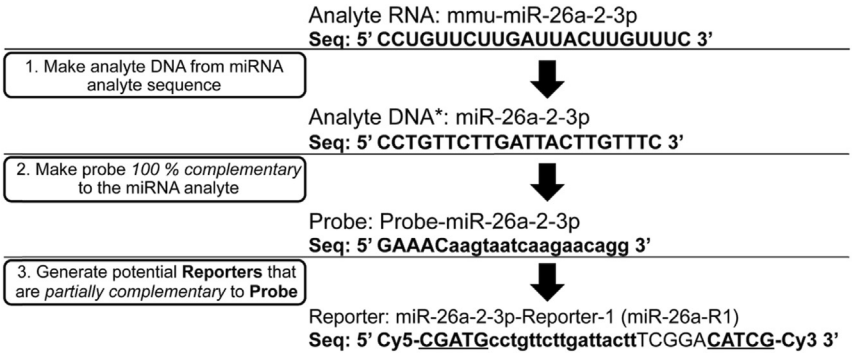

Scheme 2. Outline of the procedure to design a reporter and probe for a given miRNA analyte. Bold regions indicate complementary binding. The bold, uppercase, and underlined region of the reporter indicates the self-complementary stem. The bold and lowercase regions represent the complementary regions between the reporter and probe. The non-bold uppercase region of the reporter represents the non-complementary section of the reporter. * DNA was used instead of RNA because DNA is less susceptible to degradation and easier to work with.

the probe. Several additional filtering steps were used to remove potential reporters that may bind to the miRNA analyte and off-analytes. All of the MATLAB filtering steps were based mainly on Watson-Crick binding and brought the number of potential reporters down from thousands to tens of reporters.

The remaining reporter candidates were then more rigorously evaluated for suitable thermodynamics using freeware from the RNA Institute at SUNY Albany [41–43]. See Section 2.2 below for a more detailed description of how the thermodynamic values, molecular structures, and equilibrium concentrations of the best reporter candidates were predicted. The differences in Gibbs energy (ΔG), enthalpy (ΔH), entropy (ΔS), and melting temperature (T_m) were examined as metrics to predict if a sensor will work, as the differences drive the formation of the reporter+probe complex and subsequently the probe+analyte complex. Reporter+probe biosensors that exhibited a large negative $\Delta\Delta G$ when going from reporter+probe complex to probe+analyte complex were sought after (See Section 3.1 below for a discussion on the magnitude of the $\Delta\Delta G$ values).

To increase the stability of the reporters and combat enzymatic degradation, three locked nucleic acids (LNAs) [44,45] were strategically placed into each of the reporters. Table S1 in the supplementary information lists the sequences chosen and where the LNAs were placed. Multiple reporter designs were investigated to determine if the theoretical thermodynamic values would serve as a predictive tool for functional reporters.

Two different reporter sequences with similar thermodynamic metrics were chosen for each miRNA to investigate any alterations in biosensor functionality. Reporters miR-26a-2-R1/R2 were made for use in reporter+probe biosensors for miR-26a-2-3p. Reporters miR-27a-R1/R2 were made for use in reporter+probe biosensors for miR-27a-5p. Each biosensor was subject to miR-29b-1-5p as a common off-analyte [46]. For the remainder of this study, miR-26a-2-3p, miR-27a-5p, and miR-29b-1-5p will be referred to as miR-26a, miR-27a, and miR-29b, respectively.

The reporters contain two Cyanine (Cy) dyes, a 3′ Cy3 and a 5′ Cy5. Based on our previous work [14,15], the Cy5 dye was used as the major reporting signal. When Cy3 and Cy5 are in close proximity (primarily in the hairpin conformation), the Cy3 acts as a quencher of Cy5. Previously, we found that the Cy3-Cy5 pair does not effectively stimulate Förster Resonance Energy Transfer (FRET) enhancement with our current reporter design, but still worked in a quenching mechanism. While quenching molecules like Iowa Black Red-Quencher (IAbRQ) further reduce Cy5 emission [14], the limits of detection were not any better than using Cy3 as a quencher. The signal-off approach used here differs from molecular beacons that use signal-on, but we found that for nucleic acid biosensors the figures of merit (FOM) for signal-on and signal-off approaches were similar [14]. We have successfully made signal-on reporter+probe designs that will be the subject of future work.

All the oligonucleotides were obtained from Integrated DNA Technologies (IDT) pre-diluted in their IDTE buffer at pH 7.5 and used as received. The samples were then diluted as needed to the required concentrations in a buffer solution composed of Phosphate-buffered saline containing 10 mM Tris buffer, 2.5 mM $MgCl_2$, and 0.005% Tween 20 (final pH ~ 8). Concentrations of solutions were confirmed by a Nanodrop spectrophotometer (ND-1000).

2.2. Thermodynamic, molecular structure, and molarity fraction predictions

All predictions were performed using UNAfold freeware (a combination of mfold and DINAMelt) from SUNY Albany [41–43]. Calculations for the reporter hairpin thermodynamic values and conformations were performed using the Quikfold application under the UNAfold family. The parameters used were: DNA, 25 °C, 10 mM [Na^+], 2.5 mM [Mg^{2+}], Linear sequence type, 5% suboptimal structures, maximum of 50 foldings, no limit on distance between paired bases. Calculations for reporter+probe, probe+analyte, and other dimer hybridizations were performed using the Two State melting (hybridization) tool. The parameters used were: DNA, 25 °C, 10 mM [Na^+], 2.5 mM [Mg^{2+}], and 100 nM strand concentration.

The molarity fraction, secondary structure, and base pair probability of hairpins, homodimers, and heterodimers were calculated from DINAMelt. The 'homodimer' function was used to evaluate homodimers and the 'hybridization of two different strands' function was used to evaluate heterodimers. Different combinations of reporter, probe, and analyte were evaluated for their heterodimer or homodimer formation. To determine molarity fraction and predict secondary structure, the advanced form of the application was chosen and the energy minimization mode was selected. A temperature range of 18–40 °C was selected to span the experimentally relevant temperature window. The polymer mode was left unselected. The parameters chosen were: DNA, reporter [A_0] and probe [B_0] concentrations set to 0.1 μM (100 nM), [Na^+] concentration set to 10 mM, [Mg^{2+}] concentration set to 2.5 mM. All other settings were set to default. Secondary structures were predicted at 25 °C. Base pair probability was obtained from partition function figures using the partition function mode instead of energy minimization, but all the parameters remained the same.

2.3. Fluorimetry apparatus

A custom-built fluorimeter, previously described [15], was used to characterize the biosensors. Briefly, a titanium-sapphire ultrafast tunable laser (Mai Tai, Spectra Physics) was used to achieve two-photon excitation. The dyes were excited at 742 nm with 75 mW average power. The only difference from the instrument outlined in our earlier publication was the spectrometer. Here, a Princeton Instruments Acton SP2300 Spectrometer with a 300 grooves mm^{-1} grating blazed at 500 nm was used. Unless otherwise stated, the grating was centered at 650 nm (spectral range covered 607.569–692.347 nm, 0.165 nm $pixel^{-1}$) to look primarily at the Cy5 emission. Emission from Cy5 above 692 nm was not collected because the 705 nm long-pass dichroic mirror does not reflect wavelengths above ~690 nm to the detector. The Cy5 emission range did not contain much of the Cy3 emission peak.

The detector was a Princeton Instruments electron-multiplied CCD camera (ProEM: 512B+ eXcelon) that used LightField software with the following parameters for acquisition: 500 ms acquisition time, 3 frames, 20 frame averages, 100 kHz analog to digital conversion (ADC) speed, high analog gain, low noise ADC quality, and full frame readout, unless otherwise stated. A locking cuvette holder was installed for the 'reporter response and calibration curve' experiments outlined in experimental Section 2.4. All other experiments were conducted prior to installation of the locking cuvette holder. Samples that did not use the locking cuvette holder were susceptible to cuvette placement error due to the cuvette sitting in a different spot in the holder, leading to as much as 10–15% error [15] between replicates. The locking cuvette holder reduced inter-sample error to 1–2%.

2.4. Reporter response and calibration curves

The ability of the reporters to respond to probes and the reporter+probe biosensor's ability to respond to analyte were examined first. To show that the reporter+probe biosensors were selective for their intended analyte, two off-analytes were presented to the biosensors in the absence of analyte. No signal change upon addition of off-analytes indicated selectivity for a given biosensor. Solutions were made to contain 100 nM reporter, hybridized reporter+probe biosensor, or reporter+probe biosensor with equimolar analyte or off-analytes. A total of nine frames were obtained from 3 samples each containing 3 frames (3 frames × 3 samples = 9 frames total). The 9 frames were averaged and the standard deviation was reported as the error.

For calibration experiments, the reporter+probe solutions were prepared by hybridization of equimolar concentrations of each reporter and probe in a microcentrifuge tube. The miR-26a-R1 or miR-26a-R2 was hybridized with probe-miR-26a for at least 1 h. Hybridization of miR-27a-R1 and miR-27a-R2 with probe-miR-27a took at least 2 h. A longer reaction time was needed for miR-27a reporters with probe due to slow kinetics (Figs. S1 and S2). Aliquots of the hybridized solution were then added to another microcentrifuge tube containing analyte in enough buffer to bring the concentrations of the reporter+probe to 100 nM and 0–100 nM miRNA analyte in 20 nM increments. The reporter+probe biosensors were allowed to hybridize with the analytes for at least 1 h. All hybridizations were carried out at room temperature (~22 °C). Three calibration curves were performed for each reporter+probe biosensor (with the exception of miR-27a-R2+probe because that biosensor did not work, see Results and Discussion below).

To test for matrix effects from the off-analytes, a mixture of reporter+probe with increasing concentration of miRNA analyte and a constant concentration of two off-analytes was investigated. For all experiments each solution contained 100 nM reporter+probe, 100 nM off-analytes, and 0–100 nM analyte in 20 nM increments. The reporter+probe biosensors for miR-26a were allowed to react with analyte and off-analytes for at least 1 h before analysis. MiR-27a-R1+probe was allowed to react with analyte and off-analytes for at least 2 h before analysis. The solutions were then analyzed using the fluorimeter described above (Section 2.3).

Cy5 intensity values were obtained by summing averaged emission spectra from 620.07 nm to 690.86 nm. To determine the detection limits, the linear fit for each calibration curve was performed to 100 nM of analyte added. The intensity values of all the data points in the calibration curves were normalized to the intensity of the 100 nM reporter+probe solution without analyte. The linear fits were then forced through the y-intercept at one (the 0 nM miRNA and 100 nM reporter+probe normalized intensity), which served as the "zero" point, correlating to no analyte added. The limit of detection (LOD) was determined as $3 \times SD_{"zero"}/m$ and limit of quantitation (LOQ) was $10 \times SD_{"zero"}/m$, where $SD_{"zero"}$ was the standard deviation of the "zero" point normalized intensity and m was the slope of the calibration curve.

3. Results and discussion

3.1. Comparison of molecular structures and thermodynamics to signal change for reporter+probe biosensors

The sequences of miR-26a-R1 and miR-26a-R2 (Table S1) were different in that R1 had a longer complementary region than R2 by four bases. The first 18 bases in the reporters' sequences (from 5′ to 3′) were the same. After the 19th base the sequence '**act+t**' in R1 became 'GTG+G' in R2 decreasing the complementarity. The remainder of the non-complementary sequences in R1 and R2 were also quite different: (TC)G(G)A to (TC)C(G)T, respectively (sequence similarity indicated by parentheses).

The reporters for miR-27a (Table S1) were different in the complementary region by three bases, with the miR-27a-R1 having three more base-pairs to the probe than R2. The first nucleic acid after the 5′ stem in R1 was complementary to the probe as an Adenine, but the first nucleic after the stem in R2 was non-complementary as a Thymine. The two reporters for miR-27a had the order of Guanine and Thymine flipped at the sequence positions 16 and 17 (with R2 being flipped with respect to R1). The remainder of non-complementary sequences of R1 and R2 were also quite different: GGAC+GTTCGG vs. TCGT+CCGATT, respectively.

The four reporter designs outlined in this study were chosen because they met three criteria that we had hypothesized would result in a functional reporter+probe biosensor. First, the most probable and stable conformation of the reporter was an ideal hairpin that would bring the two dyes close enough to permit quenching (Scheme 1 and Fig. 1 and Fig. S3). Second, the melting temperature for the first reporter hairpin conformation had to be at least 10 °C above operating temperature (in this study 25 °C), and the Gibbs energy had to be about −2 kcal mol^{-1} or more negative (Table 1 and Table S2). Third, the $\Delta G_{hybridization}$ between the reporter and probe, as well as the ΔΔG between reporter+probe (R+P) and probe+analyte (P+A), had to be sufficiently large and negative to drive the reaction forward (Figs. S4 and S5 show a threshold around −10 and −5 kcal mol^{-1} for (R+P) hybridization and conversion of (R+P) to (P+A), respectively) [14,15]. These criteria also require the reporters and reporter+probe complexes minimize off-analyte interactions as described in Section 2.1 and validated in Table S3. Based on these criteria, the fewest reporter hairpins obtained for miR-26a was one. Finding just one reporter hairpin that met all the design criteria for miR-27a was more difficult and the fewest number of hairpins was three.

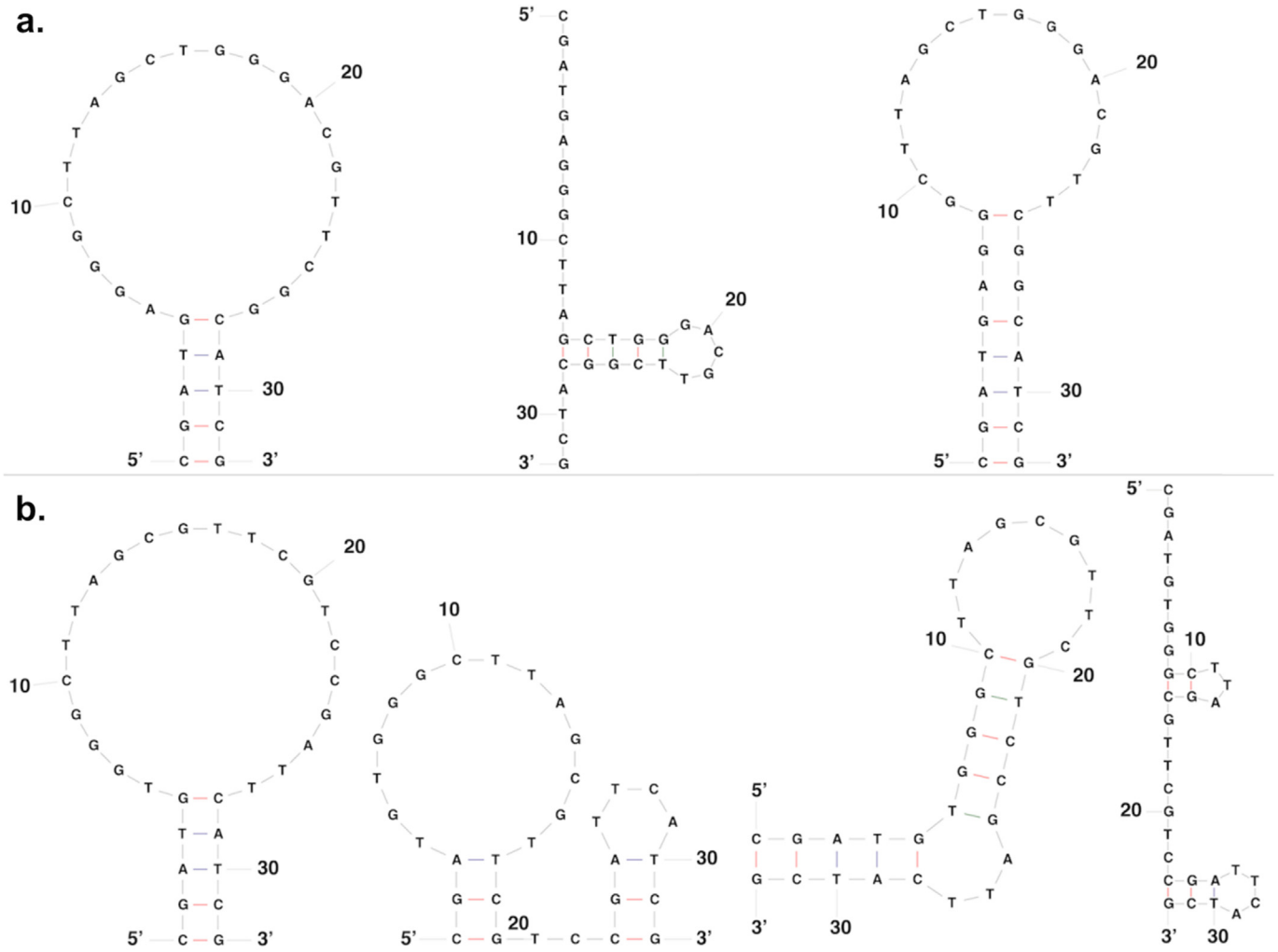

Fig. 1. Predicted miR-27a-reporter hairpin conformations in order from left to right according to decreasing stability: (a) corresponds to miR-27a-R1 with three hairpin conformations: ideal hairpin, a non-ideal hairpin, and another ideal hairpin. (b) Corresponds to miR-27a-R2 with four hairpin conformations: ideal hairpin, non-ideal hairpin, ideal hairpin, and non-ideal hairpin. Structures were obtained from Quikfold using parameters described in experimental Section 2.2. Figure does not indicate 3-dimensional structure.

Table 1 and Table S2 outline the thermodynamic values, including ΔG, ΔH, ΔS, T_m (°C), as well as the number of total base pairs, GC base pairs, and changes in base-pairs. The number of GC base pairs was included as a separate value due to their greater stability than AT pairs.

Fig. S3 and Table 1 and Table S2 reveal that miR-26a-R1 had only one stable ideal hairpin (H) but miR-26a-R2 had two stable H's. The most stable structure of both the miR-26a reporters was an ideal hairpin, in line with our initial design criteria. Recall from Scheme 1 that an ideal hairpin conformation for a reporter has the 5′ and 3′ ends of the stems close enough to cause the dyes to interact with each other and adequately quench the signal.

Fig. 1 and Table 1 and Table S2 shows that the most stable theorized conformations for the miR-27a reporters were ideal hairpins. Fig. 1 also shows the miR-27a reporters contained non-ideal hairpins as theorized stable structures. As depicted in Scheme 1, a non-ideal hairpin conformation (NH) has the two dyes further apart and causes less quenching than that of the ideal hairpin (H). Fig. 1 and Table 1 and Table S2 show that miR-27a-R1 had three conformations: H, NH, and H (in order of decreasing stability). However, miR-27a-R2 had four conformations: H, NH, H, and NH (in order of decreasing stability). The two most stable conformations of miR-27a-R2 were an ideal hairpin followed by a non-ideal hairpin, with Gibbs energies of −2.15 and −1.98 kcal mol^{-1}, respectively. The small difference in favorability between these two conformations, seen in Fig. 1b and Table S2, suggest the reporter molecules assume both ideal and non-ideal conformations in solution, or even switch back and forth between them as the molecule tests different binding motifs. This argument is strengthened by the fact that the Gibbs energy for the most stable NH of miR-27a-R2 was more stable than the most stable ideal hairpins of miR-26a-R2 and miR-27a-R1 (−1.85 and −1.95 kcal mol^{-1}, respectfully – Table S2).

Table 1 and Fig. S4 shows the thermodynamic values, total base pairs, and changes in base pairs associated with reporter+probe complex formation for each of the four reporters. From a thermodynamic standpoint, miR-27a-R2+probe complex was the least stable. The low thermodynamic stability of miR-27a-R2+probe was likely due to it containing the fewest number of predicted base pairs and changes in base pairs amongst all the reporters. From Table 1, miR-27a-R2 had nine base pairs and depending on the ideal hairpin structure, but only gained four or lost one base pair upon complex formation (based on ideal hairpin base pairs).

Table S4 shows the thermodynamic values and base pairs associated with forming probe+analyte complexes. Table 1 and Fig. S5 show that among the reporters, miR-26a-R1 had the

Table 1
Comparison of thermodynamic values and molecular structure information for reporter hairpins, reporter+probe complexes, and conversion of reporter+probe complexes to probe+analyte complexes.

	miR-26a-R1	miR-26a-R2	miR-27a-R1	miR-27a-R2
ΔG(R)* kcal mol^{-1}	−2.33	−1.85	−1.95	−2.15
ΔH(R)* kcal mol^{-1}	−55.4	−37.8	−37.9	−40.6
ΔS(R)* cal mol^{-1} K^{-1}	−178	−120.58	−120.58	−128.96
T_m(R)* °C	38.1	40.3	40.3	41.7
Number of predicted reporter structures	1	2	3	4
H:NH	1:0	2:0	2:1	2:2
Total base pairs in R*	7	5 (7**)	5(6**)	5(10**)
Total base pairs in RP	17	13	12	9
ΔBases R-(1st hairpin)* to RP	+10	+8(+5**)	+7(+6**)	+4 (−1**)
R-Homodimer Tm	−4.6	−9	14.8	15.7
R-hairpin to R-homodimer probability	Hairpin > Homodimer	Hairpin ~ Homodimer	Hairpin ~ < Homodimer	Hairpin < Homodimer
Total number of base pairs in R-homodimer	5	5	10	24
ΔBases homodimer to RP	+12	+8	+2	−15
ΔG(RP) kcal mol^{-1}	−19.8	−16.1	−16.9	−12.9
ΔH(RP) kcal mol^{-1}	−126.8	−107.5	−98.1	−83.1
ΔS(RP) cal mol^{-1} K^{-1}	−359	−306.4	−272.5	−235.5
T_m(RP) °C	48.9	41.9	46.1	34.3
ΔΔG(RP to PA) kcal mol^{-1}	−5.5	−9.2	−14.2	−18.2
ΔΔH(RP to PA) kcal mol^{-1}	−41.5	−60.8	−80.7	−95.7
ΔΔS(RP to PA) cal mol^{-1} K^{-1}	−120.5	−173.1	−223.1	−260.1
ΔT_m (RP to PA) °C	5.2	12.2	17.9	29.7
ΔBase pairs (RP to PA)	5	9	8	11

*=most stable ideal hairpin,** = second stable ideal hairpin. H = ideal hairpin and NH = non-ideal hairpin.

smallest changes in base pairs and melting temperature upon conversion from reporter+probe to probe+analyte, but the most positive-but still negative-ΔΔG, ΔΔH, and ΔΔS. In contrast, miR-27a-R2 had the largest changes in base pairs and melting temperature as well as the most negative ΔΔG, ΔΔH, and ΔΔS. Recall large magnitudes in ΔΔG, ΔΔH, ΔΔS, ΔT_m, and changes in base pairs were desired to push the reaction forward, provided the reporter+probe formed.

Considering the thermodynamic and base pairing analysis described above, we expected all the reporters to form reporter+probe complexes and function as biosensors. In fact, from a thermodynamic standpoint we expected miR-27a-R2 to work the best. However, Fig. 2 shows this was not the case.

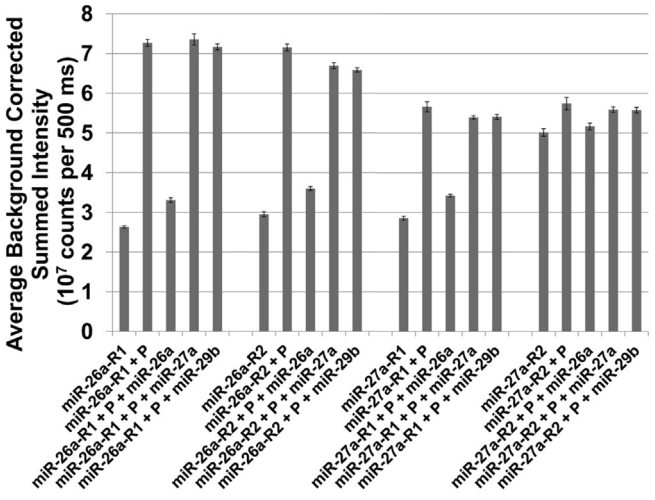

Fig. 2. Reporter response to probe and reporter+probe response to analytes and off-analytes (n = 9). Each reporter+probe biosensor was sensitive to equimolar analyte, and not sensitive towards off-analytes.

To understand how the difference in sequence, molecular structure, and thermodynamic values for each reporter affected their performance as part of a biosensor, we evaluated the reporter signal change before and after adding probe and then analyte (Fig. 2). The experimental baseline signal from each reporter was an average from the hairpin sampling different conformations accompanied by opening and closing of the hairpin as the hairpins are not static. While the dynamic nature of the hairpin causes varying amounts of fluorescent signal, the detection volume contained many reporters in various conformations that change states on time scales faster than the acquisition time. Thus, the signal from a given reporter was stable (~1–3% RSD) over the acquisition times used in this work.

Comparison of the hairpin signal among the different reporters in Fig. 2 reveals that a reporter with more than one predicted hairpin did statistically increase the baseline signal (95% confidence interval, n = 9). Ideal hairpins for the reporters demonstrated quenched fluorescence ~3 × 10^7 counts per 500 ms, but the extent of quenching depended on the proximity and orientation of the dyes. If a NH forms as much or more than an H (Scheme 1 and Fig. 2), then less quenching will occur resulting in more fluorescence observed from the dyes on the reporter (~5 × 10^7 counts per 500 ms for miR-27a-R2). Both miR-26a-R2 and miR-27a-R1 had more than one H and signals near 3 × 10^7 counts per 500 ms, but miR-27a-R1 had one NH – as the second stable structure – compared to no NH's for miR-26a-R2. From these results, the presence of a NH alone – as a second stable structure – did not raise the reporter baseline signal above that of a reporter with two H's.

Signal change from the reporter before and after probe addition was used to determine the expected signal change from the reporter+probe biosensor in the presence of miRNA. Addition of probe to reporter also served as a control to confirm the probe

opened the hairpin. Upon probe binding the intensities of miR-26a-R1 and miR-26a-R2 increased by 176 ± 4% and 142 ± 4%, respectively. Addition of probe to miR-27a-R1 and miR-27a-R2 caused the signal to increase by 98 ± 5% and 14 ± 4%, respectively. A similar trend in percent signal change was observed upon miRNA addition: 120 ± 4% (miR-26a-R1), 99 ± 3% (miR-26a-R2), 65 ± 4% (miR-27a-R1), and 11 ± 3% (miR-27a-R2). Of these changes in signal, miR-27a-R2 was the smallest, but statistically significant ($p < 0.05$, $n = 9$). Preliminary data of the discrepancies between the percent changes in signal from reporter hairpin to reporter+probe and reporter+probe to reporter hairpin after miRNA addition suggest the biosensors were about 70% quantitative. A follow-up manuscript is under preparation that investigates this discrepancy in more detail.

One major difference observed among the reporters was that miR-27a-R2 had a baseline signal that was over ~1.7 times greater than the other reporter hairpin signals in Fig. 2. Considering the large baseline signal from miR-27a-R2, along with the evidence that the reporter hairpin had a similar intensity to the other reporter+probe complexes (~5×10^7 counts per 500 ms), suggested that on average the dyes were far apart for miR-27a-R2 alone. However, Fig. S6 shows all reporters had low Cy3 relative to Cy5, suggesting a structure with the dyes close to one another. Thus, the miR-27a-R2 must have dyes close enough for quenching, but not close enough to fully quench the Cy3 and Cy5 emission. From the experimental data in Fig. 2, Fig. S6, and the predicted Gibbs energies of the H and NH, we hypothesize that the high baseline signal from miR-27a-R2 came from an equilibrium between the most stable H and NH conformations of the reporter.

To further support the structure of miR-27a-R2, both the miR-27a-R2 hairpin and reporter+probe complex exhibited about a 5 nm red shift in the Cy5 emission with respect to the other reporters (Fig. S7). A red shift in the Cy5 emission arises from the molecular environment that the Cy5 exists in and has previously been traced to interactions between DNA and cyanine dyes [47]. The observed red shift confirms the miR-27a-R2 had a different structure than the other reporters. See Fig. S6 to S9 for more evidence and discussion regarding the structure of miR-27a-R2 compared to other reporters as a hairpin and complexed to probe.

Another possible state miR-27a-R2 may have existed in was a homodimer. We looked into the occurrence of possible homodimers that could be affecting the signal of the reporter (Fig. 3 and Table 1 and Table S5). Amongst all of the reporters in Table S5, miR-27a-R2 formed the second most stable homodimer in terms of Gibbs energy (−5.6 kcal mol^{-1}, miR-27a-R1 was the most stable) and the most stable in terms of enthalpy ($\Delta H = -122.2$ kcal mol^{-1}), melting temperature (15.7 °C), and number of base pairs (24 total and 14 GC).

While the miR-27a-R2 homodimer was favored by Gibbs energy and enthalpy, it was not favored by entropy ($\Delta S = -391$ cal mol^{-1} K^{-1}) and the melting temperature was below room temperature (15.7 °C). Since the reporter did have locked nucleic acids that likely increased the melting temperature near to room temperature, combined with the 24 base pairs in the homodimer, suggests a homodimer may have formed. However, the high Cy5 signal (~5×10^7 counts per 500 ms) observed did not support the predicted reporter homodimer structure (Fig. 3c) as a major product because the Cy3 and Cy5 would be next to each other much like an ideal hairpin, quenching the signal. Instead, the homodimer may be dynamically forming and unforming such that the Cy3 and Cy5 are not close enough to fully quench the signal. All the results for miR-27a-R2 presented support the claim that it exists in many states including a dynamic homodimer along with the two ideal and two non-ideal hairpin conformations.

While reporters may form homodimers, the biosensor can still function provided the probe can react with a reporter to form a reporter+probe complex and change the signal. Comparing the conversion of reporter homodimers to reporter+probe complexes in Fig. S10 reveals some key differences between miR-27a-R2 and the other reporters. Mainly the conversion of miR-27a-R2 homodimer to reporter+probe was the most positive in terms of ΔΔG (about −7 kcal mol^{-1}) and the change in melting temperature was the smallest (~19 °C). In addition, the process was endothermic and resulted in the loss of 15 base pair interactions (Fig. S10).

To better understand the structural states of miR-27a-R2 and how it could affect the biosensor functionality, we compared the energy minima predicted structures and probability maps of miR-27a-R2 to the reporter that worked the best (miR-26a-R1). Figs. 3 and 4 show the theorized interaction structures (a–c) and probabilities (d–f) between reporter hairpin, reporter+probe, and reporter homodimer for miR-27a-R2 and miR-26a-R1, respectively. In (d–f) of Figs. 3 and 4, increasing size and color change from cold (blue) to hot (red) followed increasing probability (The color code key for the probability maps can be found in Fig. S11).

Comparison of Fig. 3d to 3f reveals that the homodimer had large green boxes compared to the smaller light green boxes of the hairpin, suggesting that the homodimer was more probable for miR-27a-R2. Now compare the most stable NH of miR-27a-R2 from Fig. 1b at positions 23, 24, and 25 to those positions in the probability map of Fig. 3d. Note the hairpin in Fig. 3d had positions 23, 24, and 25 bound to positions 32, 31, and 30, respectively with large green boxes suggesting a highly probable state (the green boxes indicate over 50% probability). We will use a bullet (•) to represent binding between two base pair positions. The 23•32, 24•31, and 25•30 binding positions were present in both the most and least stable NH. The most stable NH also had positions 18•3, 19•2, and 20•1 binding but with small teal boxes that were about 20% probable. The other NH also had positions 9•15 and 10•14 bound with 10–20% probability. Finally, the most stable ideal hairpin had small light green boxes indicating 30–50% probability in the stem. The variety of probable hairpin structures was the main basis to suspect the non-ideal hairpins were in equilibrium with ideal hairpins. In fact the most stable NH was likely as probable if not more probable than the most stable H. This analysis of H and NH probabilities combined with the observed signals in Fig. 2 and low melting temperature of the homodimer (Table S5) suggest the homodimer will most likely not form in large amounts despite the high predicted probability. Any small amount of homodimer that may form will likely restrict formation of reporter+probe because such a process was endothermic and decreased the number of base pairs formed (Table S5 and Fig. S10). Considering the small change in signal upon probe binding for miR-27a-R2 in Fig. 2 in relation to Fig. 3b and 3e show that even with highly (over 90%) probable base pairs in the reporter+probe complex, probability alone was not enough to predict reporter+probe complex formation.

The stability of a miR-27a-R1 homodimer was predicted to be $\Delta G = -6.5$ kcal mol^{-1}, $\Delta H = -84.8$ kcal mol^{-1}, $\Delta S = -262.5$ cal mol^{-1} K^{-1}, $T_m = 14.8$ °C, 10 base pairs, and 6 GC base pairs (Table S5). In terms of probability, the homodimer was predicted to be as or slightly more probable than the hairpin (Fig. S12). Moreover, examination of the equilibrium between homodimer and reporter+probe heterodimer for miR-27a-R1 reveals the ΔΔH and ΔΔS were −13.39 kcal mol^{-1} and -10 cal mol^{-1} K^{-1} (Fig. S10). While presence of homodimers may have contributed to issues with the kinetics of miR-27a reporters, there were some key differences between the homodimers for miR-27a-R1 and R2. The magnitudes of ΔH and ΔS for miR-27a-R1 were smaller than miR-27a-R2 by about 35 kcal mol^{-1} and 130 cal mol^{-1} K^{-1}, respectively (Table S5). The big difference was in the base pair interactions with 10 (6 GC) for miR-27a-R1 compared to 24 (14 GC) for miR-27a-R2. While a miR-27a-R1 homodimer may

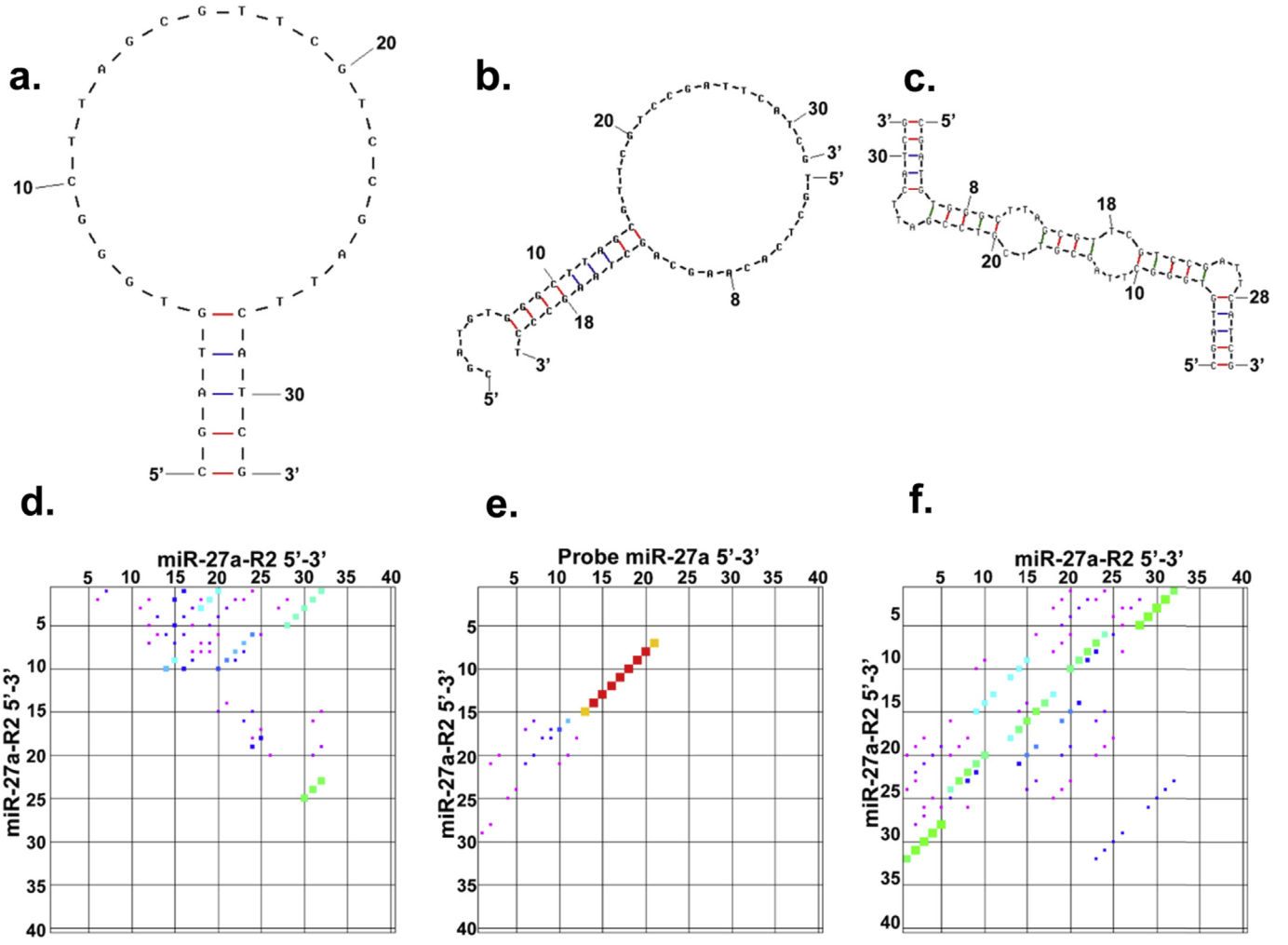

Fig. 3. Energy minima structures and partition function probability maps for miR-27a-R2. The predicted energy minima structures for (a) miR-27a-R2 folded, (b) miR-27a-R2+Probe complex, and (c) miR-27a-R2 homodimer, respectively, at 25 °C. Figure does not indicate 3-dimensional structure. (d)–(f) are partition function probability maps that correspond to energy minima structures (a)–(c), respectively. (Size and color of dots in partition function probability map indicate probability). The largest boxes are the most probable base pairs. For the color, the probability increases from violet (least probable) to red (most probable). See Fig. S11 for probability maps color code. Structures and probability maps were obtained using parameters described in experimental Section 2.2. (For interpretation of the references to colour in this figure legend, the reader is referred to the web version of this article.)

form, the fact there were fewer base pairs in the homodimer, a gain in base pairs on reporter+probe formation, and the reporter+probe formation was exothermic, unlike R2, suggests a reporter+probe complex will still form with miR-27a-R1. The melting temperatures of the miR-27a reporters were similar near 15 °C, but probably closer to room temperature with the locked nucleic acids. The ~3 × 10^7 counts per 500 ms for miR-27a-R1 did not support the predicted homodimer structure. Thus melting temperature alone cannot help determine if a homodimer will or will not form.

In Fig. 4, the miR-26a-R1 reporter hairpin had large green boxes compared to smaller light green boxes of the homodimer, suggesting hairpin formation was more probable. Hairpin formation for miR-26a-R1 was supported by its observed relatively low signal (~3 × 10^7 counts per 500 ms) and high melting temperature (38.1 °C). (Similar probability maps for miR-26a-R2 can be found in Fig. S13).

Fig. 5 shows the predicted molarity fraction of each species from the UNAfold 'Hybridization of two different strands' function. Fig. 5a and 5b shows both miR-26a-R1 and R2 had a majority (above 95%) of the reporter and probe molecules complexed at 25 °C. Fig. 5c shows ~85% of the species were miR-27a-R1+probe complexes. These large percent formations were reflected in the observed signal changes of Fig. 2. The fact that miR-27a-R1 had ~10% of the reporters in the hairpin structure explains why the signal change of Fig. 2 was not greater than ~98% upon probe addition. The molarity fraction in Fig. 5d shows that only ~5% of the solution was predicted to contain miR-27a-R2+probe complex, at 25 °C. A majority of the species were free reporters and probes. The fact that miR-27a-R2+probe was predicted to form in a small amount was in-line with the observed small ~14% signal change in Fig. 2.

Considering Fig. 2 in relation to Fig. 5, the molarity fraction calculation from 'Hybridization of two different strands' was an excellent tool to predict extent of reporter+probe formation. Figs. S6, S8, and S9 further explore the relationships between Figs. 2 and 5 by examining reporter+probe complex formation upon addition of 1×, 2×, and 100× probe to each of the reporters.

There were a few major problems with the molarity fraction tool. One problem was that it assumes a nucleic acid molecule that can form hairpins cannot form a homodimer complex, no matter how stable or probable. This assumption weakens the capabilities of the molarity fraction tool for the purpose of reporter design

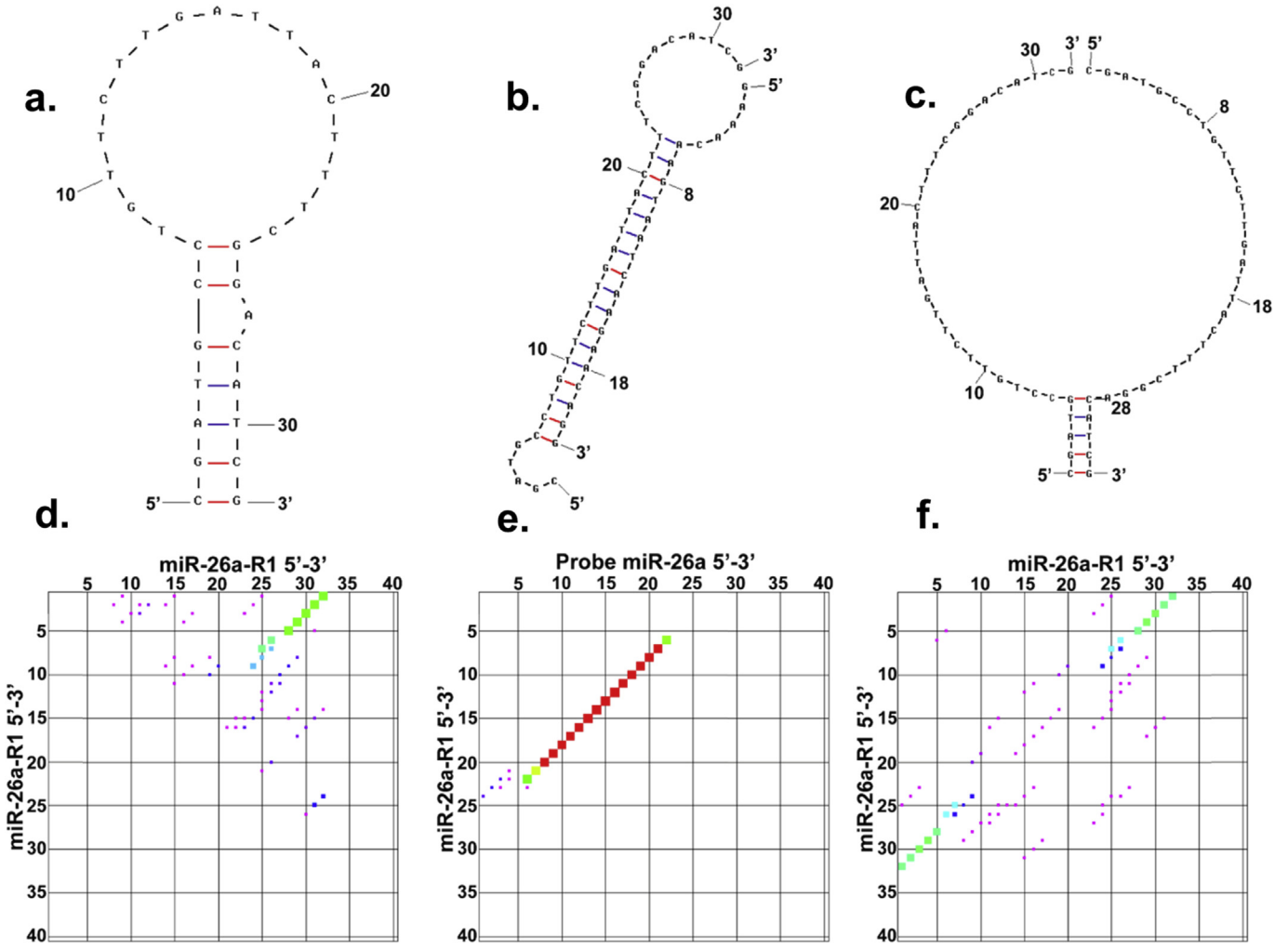

Fig. 4. Energy minima structures and partition function probability maps for miR-26a-R1. The predicted energy minima structures are for (a) miR-26a-R1 folded, (b) miR-26a-R1+Probe complex, and (c) miR-26a-R1 homodimer, respectively, at 25 °C. Figure does not indicate 3-dimensional structure. (d)–(f) are partition function probability maps that correspond to energy minima structures (a)–(c), respectively. (Size and color of dots in partition function probability map indicate probability). The largest boxes are the most probable base pairs. For the color, the probability increases from violet (least probable) to red (most probable). See Fig. S11 for probability maps color code. Structures and probability maps were obtained using parameters described in experimental Section 2.2. (For interpretation of the references to colour in this figure legend, the reader is referred to the web version of this article.)

because it does not provide insight into the extent of homodimer formation. Another limitation was only one reporter and probe at a time could be analyzed. Thus molarity fraction analysis was only useful near the end of the design process, when there were only a handful of reporters to investigate further.

Comparison of predicted and experimental data reveals that thermodynamics, molecular structure, and predicted equilibrium concentrations need to be analyzed as a whole rather than independently. For example, while the reporter hairpin and reporter+probe complex for miR-27a-R2 showed the worst-case scenario, it was the best for reporter+probe to probe+analyte conversion in terms of thermodynamics. From the analysis here, we found molecular structure, thermodynamic metrics, reporter+probe equilibrium concentrations, changes in base pairs, and homodimer probabilities were key to selecting an optimal reporter.

In summary, to design a reporter for reporter+probe biosensors, first generate reporter candidates based on the probe such that off-analyte interactions are minimized. Second, perform thermodynamic analysis to further reduce off-analyte interactions and ultimately reduce the number of reporters. Third, evaluate changes in base pairs upon reporter+probe formation. Fourth, assess the predicted reporter hairpin and homodimer structures. Fifth, evaluate equilibrium molarity fractions of different reporters with their probe. Finally, compare thermodynamics and changes in base pairs upon probe+analyte formation.

Below is a summary of some design principles from Table 1 for 100 nM reporter (R), 100 nM probe (P), and 100 nM analyte (A) at an operating temperature of 25 °C:

1. The most probable and thermodynamically stable conformation of the reporter must be an ideal hairpin.
2. Reporter Hairpin
   a. Molecular Structure Metrics
      i. Number of predicted structures: as few as possible.
         1. Just one H
         2. H > NH
      ii. Total number of hairpin base pairs depends more on difference in base pairs from R to RP
         1. Total base pairs: 5 to 7
         2. Change in base pairs (R to RP) $\geq$ 6

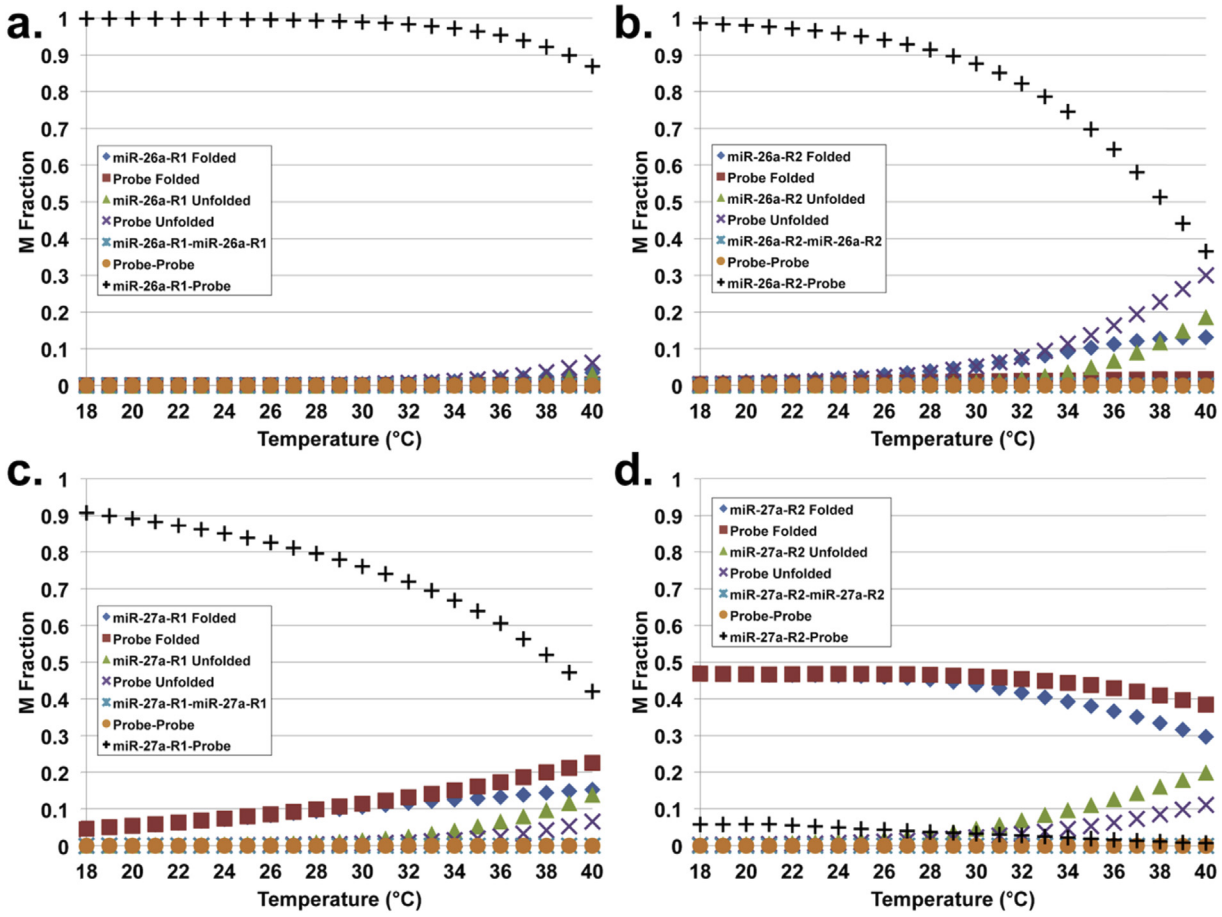

Fig. 5. Molarity fraction of each of the reporters with their respective probes. The molarity of each structure formed was divided by the total molarity of each individual substance. (a) miR-26a-R1, (b) miR-26a-R2, (c) miR-27a-R1, and (d) miR-27a-R2. The reporter+probe complex was predicted to form in great abundance at room temperature (>90%) in (a) and (b) but not (c) and (d). Molarity fractions were obtained from 'Hybridization of two different strands' using parameters described in experimental Section 2.2.

   b. Thermodynamic Metrics: most stable hairpin thermodynamic metrics (with at least one locked nucleic acid in the stem)
      i. $\Delta G_{hairpin}$: -1.85 kcal mol^{-1} or more negative.
      ii. $\Delta H_{hairpin}$: -37.8 kcal mol^{-1} or more negative.
      iii. $\Delta S_{hairpin}$: -120.58 cal mol^{-1} K^{-1} or more positive.
      iv. $T_{m,\ hairpin} \geq 40.3$ °C (18 °C above operating temperature, a melting temperature of 38 °C is acceptable provided $\Delta G_{hairpin} \leq -2.33$ kcal mol^{-1} and $\Delta H_{hairpin} \leq -55.4$ kcal mol^{-1})
3. Reporter+Probe (with at least two locked nucleic acids in the loop)
   a. Molecular Structure Metrics
      i. Total number of base pairs depends on number of base pairs in stem of reporter. (See principle 2.a.ii.1)
         1. For a reporter with a 5 base pair stem, the RP complex should have at least 11 base pairs.
   b. Thermodynamic Metrics
      i. ΔG_{RP}: -16.1 kcal mol^{-1} or more negative.
      ii. ΔH_{RP}: -98.1 kcal mol^{-1} or more negative.
      iii. ΔS_{RP}: -272.5 cal mol^{-1} K^{-1} or more positive.
      iv. $T_{m,RP} \geq 41.9$ °C (20 °C above operating temperature)
   c. Percent reporter+probe formation
      i. over 95%
4. conversion of (R+P) to (P+A)
   a. Molecular Structure Metrics
      i. Total number of RP base pairs depends more on difference in base pairs from RP to PA
         1. Change in Base Pairs (RP to PA): gain of at least 5 base pairs
   b. Thermodynamic Metrics
      i. $\Delta\Delta G$: -5 kcal mol^{-1} or more negative.
      ii. $\Delta\Delta H$: -41.5 kcal mol^{-1} or more negative.
      iii. $\Delta\Delta S$: -120.5 cal mol^{-1} K^{-1} or more positive.
      iv. $\Delta T_m > 5.2$ °C
5. Homodimer considerations for reporters and probes:
   a. While one type of homodimer (reporter+reporter or probe+probe) is tolerable, one or more runs the risk of slowing the kinetics of reporter+probe formation. If possible, homodimers of reporters and probes should be avoided. The probability and thermodynamics of the homodimer formation should not be favorable.
   b. Molecular Structure Metrics
      i. The probability of a reporter hairpin or probe single strand must be greater than or about the same as the homodimer
      ii. Change bases from homodimer to RP ≥ 2
   c. Thermodynamic Metrics:
      i. $\Delta G_{homodimer}$: -7.5 kcal mol^{-1} or more positive.
      ii. $\Delta H_{homodimer}$: -93.65 kcal mol^{-1} or more positive.
      iii. $\Delta S_{homodimer}$: -262.5 cal mol^{-1} K^{-1} or more negative.
      iv. $T_{m,\ homodimer} < 15$ °C

The summary of design principles are best for use with fixed cells and tissue. However, these metrics can be extended to other temperatures. For analysis in cells or *in vivo* at 37 °C, the number of base pairs in the reporter hairpin and reporter+probe will likely need to be increased to achieve similar thermodynamic values as outlined above and in Table 1. If the same ΔG value can be obtained at 37 °C, then the equilibrium constants for the various species will increase by about 16%. At elevated temperatures, the reporters should give functional reporter+probe biosensors provided the magnitude of changes in base pairs and thermodynamic values are in the same range as those summarized above and in Table 1.

3.2. Analytical figures of merit for reporter+probe biosensors

The reporter+probe biosensors for miR-26a and miR-27a had LODs that ranged from 5 to 9 nM (Table S6). Table S6 shows the sensitivity (slopes) and limits of detection and quantitation (LOD and LOQ) derived from the calibration curves for the biosensors in this study. The linear dynamic ranges of the biosensors were fit from 0 to 100 nM analyte added. LOD can be improved by decreasing the reporter+probe concentrations. We have previously demonstrated that decreasing the concentration of the reporter+probe complex to 500 pM gave an LOD of 49.38 ± 1.77 pM [14]. A calibration curve was performed using miR-27a-R2+probe out to 100 nM miR-27a, but the slope was non-linear and small due to the ~11% decrease in signal between reporter+probe and reporter, upon addition of analyte. The percent relative standard deviation (RSD) for the LOD and LOQ ranged from 10 to 67%. This error was a reflection of the sample preparation error rather than the sensor itself.

Comparison of the sensitivity from analysis of the calibration curve slopes and derived LOD/LOQ in Table S6 with and without the addition of off-analytes to each reporter showed no significant difference at the 95% confidence interval. The fact that the slopes and detection limits were similar with and without off-analytes indicated the biosensors were selective for their analyte. Comparison of the slopes between the reporters for miR-26a and miR-27a reveal a factor of about 1.26× difference. This change in slope was attributed to the larger maximum signal change for the miR-26a reporters with respect to miR-27a-R1 (over 90% compared to ~65%, respectively).

4. Conclusions

This work outlines design procedures and the design principles to make reporters for reporter+probe biosensors. Specifically reporter+probes for miR-26a and miR-27a were made and showed a dynamic range from 5 to 100 nM. Analysis of the calibration data showed that reporters with a maximum signal difference from 65% to 120% gave comparable detection limits and dynamic ranges. The fact that these biosensors demonstrated excellent selectivity in the presence of off-analytes will be of great value for future use in cellular and tissue matrices. Despite the semi-quantitative (~70%) nature of the sensors, the responses to concentration were reproducible (1–2%).

Predicting reporters that will bind probe and get displaced from probe when miRNA analyte is present is not trivial. Furthermore, reporters that will have maximum signal change between the open reporter+probe state and the closed reporter stem-loop hairpin conformation are difficult to identify. Many thermodynamic, molecular structure, and equilibrium concentration considerations need to be taken into account when picking the reporter sequence that will result in a functional biosensor. While only 3 out of the 4 reporters were functional, the poor functionality of miR-27a-R2 allowed discovery of key design principles for these displacement based reporters with self-complementarity.

From this study, we have found additional guidelines (in addition to the original three) to follow when designing reporter+probe biosensors. A good reporter will have an ideal stem-loop hairpin conformation that brings the dyes close together as the most stable structure and limits the number of non-ideal hairpins. Minimizing the stability and probability of potential homodimers of the reporter and probe is an important design criterion to ensure formation of the reporter+probe complex. A solution of reporter and probe should consist of over 95% reporter+probe. When considering the change in thermodynamics amongst reporter hairpins and subsequent formation of the reporter+probe complexes, ΔG, ΔH, ΔS, T_m and base pairs (related to ΔH and ΔS) must be evaluated simultaneously. These guidelines are important when designing sensors that use a displacement mechanism since being confident that a sequence will work as intended before purchasing will save time and decrease cost.

Looking towards the future, we will study the kinetics of analyte binding to reporter+probe biosensors. Other chemical modifications will be incorporated into the reporter to reduce chances of stems and non-complementary regions binding to endogenous RNA, DNA, and to ensure no interaction with off-analytes. Another consideration for the stem sequences is that they should be customized to each reporter to avoid the stem complexing to the probe or analyte. We will use these technologies to design reporter+probe biosensors that can be delivered into cells and tissue for *in situ* miRNA analysis.

Acknowledgments

We would like to acknowledge Oregon State University start-up funds for supporting this work. The OSU Research Office is also acknowledged for support through the General Research Fund. Nicholas was supported by the Dorothy and Ramon Barnes Research Fellowship.

Appendix A. Supplementary data

Supplementary data related to this article can be found at http://dx.doi.org/10.1016/j.aca.2015.12.040.

References

[1] C.M. Croce, Causes and consequences of microRNA dysregulation in cancer, Nat. Rev. Genet. 10 (2009) 704–714, http://dx.doi.org/10.1038/nrg2634.
[2] Y. Liang, D. Ridzon, L. Wong, C. Chen, Characterization of microRNA expression profiles in normal human tissues, BMC Genomics 8 (2007) 166, http://dx.doi.org/10.1186/1471-2164-8-166.
[3] T. Subkhankulova, M.J. Gilchrist, F.J. Livesey, Modelling and measuring single cell RNA expression levels find considerable transcriptional differences among phenotypically identical cells, BMC Genomics 9 (2008) 268, http://dx.doi.org/10.1186/1471-2164-9-268.
[4] C. Ragan, M. Zuker, M.A. Ragan, Quantitative prediction of miRNA-mRNA interaction based on equilibrium concentrations, PLoS Comput. Biol. 7 (2011), http://dx.doi.org/10.1371/journal.pcbi.1001090.
[5] L.F. Sempere, Tissue slide-based microRNA characterization of tumors: how detailed could diagnosis become for cancer medicine? Expert Rev. Mol. Diagn. 14 (2014) 853–869, http://dx.doi.org/10.1586/14737159.2014.944507.
[6] J. Shum, N. Paul, Chemically modified primers for improved multiplex polymerase chain reaction, Anal. Biochem. 388 (2009) 266–272, http://dx.doi.org/10.1016/j.ab.2009.02.033.
[7] J. Hanna, H. Wimberly, S. Kumar, F. Slack, S. Agarwal, D. Rimm, Quantitative analysis of microRNAs in tissue microarrays by in situ hybridization, BioTechniques 52 (2012), http://dx.doi.org/10.2144/000113837.
[8] X. Zhang, Y. Song, A.Y. Shah, V. Lekova, A. Raj, L. Huang, M.A. Behlke, A. Tsourkas, Quantitative assessment of ratiometric bimolecular beacons as a tool for imaging single engineered RNA transcripts and measuring gene expression in living cells, Nucleic Acids Res. 41 (2013) e152, http://dx.doi.org/10.1093/nar/gkt561.
[9] G.V. Glinsky, RNA-guided diagnostics and therapeutics for next-generation individualized nanomedicine, J. Clin. Investig. 123 (2013) 2350–2352, http://dx.doi.org/10.1172/JCI69268.
[10] J.B. Sternberg, N.A. Pierce, Exquisite sequence selectivity with small

conditional RNAs, Nano Lett. 14 (2014) 4568–4572, http://dx.doi.org/10.1021/nl501593r.
[11] M. de Planell-Saguer, M.C. Rodicio, Detection methods for microRNAs in clinic practice, Clin. Biochem. 46 (2013) 869–878, http://dx.doi.org/10.1016/j.clinbiochem.2013.02.017.
[12] A.K. Chen, O. Davydenko, M.A. Behlke, A. Tsourkas, Ratiometric bimolecular beacons for the sensitive detection of RNA in single living cells, Nucleic Acids Res. 38 (2010) e148, http://dx.doi.org/10.1093/nar/gkq436.
[13] J.J. Li, R. Geyer, W. Tan, Using molecular beacons as a sensitive fluorescence assay for enzymatic cleavage of single-stranded DNA, Nucleic Acids Res. 28 (2000) e52, http://dx.doi.org/10.1093/nar/28.11.e52.
[14] C.K. Almlie, N.E. Larkey, S.M. Burrows, Fluorescent microRNA biosensors: a comparison of signal generation to quenching, Anal. Methods 7 (2015) 7296–7310, http://dx.doi.org/10.1039/C5AY00504C.
[15] N.E. Larkey, C.K. Almlie, V. Tran, M. Egan, S.M. Burrows, Detection of miRNA using a double-strand displacement biosensor with a self-complementary fluorescent reporter, Anal. Chem. 86 (2014) 1853–1863, http://dx.doi.org/10.1021/ac403866g.
[16] T.D. Schmittgen, A high-throughput method to monitor the expression of microRNA precursors,, Nucleic Acids Res. 32 (2004) e43, http://dx.doi.org/10.1093/nar/gnh040.
[17] T.D. Schmittgen, E.J. Lee, J. Jiang, A. Sarkar, L. Yang, T.S. Elton, C. Chen, Real-time PCR quantification of precursor and mature microRNA, Methods 44 (2008) 31–38, http://dx.doi.org/10.1016/j.ymeth.2007.09.006.
[18] W. Li, K. Ruan, MicroRNA detection by microarray, Anal. Bioanal. Chem. 394 (2009) 1117–1124, http://dx.doi.org/10.1007/s00216-008-2570-2.
[19] P. Santangelo, N. Nitin, G. Bao, Nanostructured probes for RNA detection in living cells, Ann. Biomed. Eng. 34 (2006) 39–50, http://dx.doi.org/10.1007/s10439-005-9003-6.
[20] N. Srinivas, T.E. Ouldridge, P. Šulc, J.M. Schaeffer, B. Yurke, A.A. Louis, J.P.K. Doye, E. Winfree, On the biophysics and kinetics of toehold-mediated DNA strand displacement, Nucleic Acids Res. 41 (2013) 10641–10658, http://dx.doi.org/10.1093/nar/gkt801.
[21] E.A. Lesnik, S.M. Freier, Relative thermodynamic stability of DNA, RNA, and DNA: RNA hybrid duplexes: relationship with base composition and structure, Biochemistry 34 (1995) 10807–10815, http://dx.doi.org/10.1021/bi00034a013.
[22] N. Sugimoto, S. Nakano, M. Yoneyama, K. Honda, Improved thermodynamic parameters and helix initiation factor to predict stability of DNA duplexes, Nucleic Acids Res. 24 (1996) 4501–4505, http://dx.doi.org/10.1093/nar/24.22.4501.
[23] R.A. Dimitrov, M. Zuker, Prediction of hybridization and melting for double-stranded nucleic acids, Biophys. J. 87 (2004) 215–226, http://dx.doi.org/10.1529/biophysj.103.020743.
[24] C. Chen, W. Wang, Z. Wang, F. Wei, X.S. Zhao, Influence of secondary structure on kinetics and reaction mechanism of DNA hybridization, Nucleic Acids Res. 35 (2007) 2875–2884, http://dx.doi.org/10.1093/nar/gkm177.
[25] G. Bonnet, O. Krichevsky, A. Libchaber, Kinetics of conformational fluctuations in DNA hairpin-loops, Proc. Natl. Acad. Sci. 95 (1998) 8602–8606.
[26] A.E. Pasquinelli, B.J. Reinhart, F. Slack, M.Q. Martindale, M.I. Kuroda, B. Maller, D.C. Hayward, E.E. Ball, B. Degnan, P. Müller, J. Spring, A. Srinivasan, M. Fishman, J. Finnerty, J. Corbo, M. Levine, P. Leahy, E. Davidson, G. Ruvkun, Conservation of the sequence and temporal expression of *let-7* heterochronic regulatory RNA, Nature 408 (2000) 86–89, http://dx.doi.org/10.1038/35040556.
[27] A.E. Pasquinelli, A. McCoy, E. Jiménez, E. Saló, G. Ruvkun, M.Q. Martindale, J. Baguñà, Expression of the 22 nucleotide *let-7* heterochronic RNA throughout the Metazoa: a role in life history evolution? Evol. Dev. 5 (2003) 372–378, http://dx.doi.org/10.1046/j.1525-142X.2003.03044.x.
[28] S. Roush, F.J. Slack, The *let-7* family of microRNAs, Trends Cell Biol. 18 (2008) 505–516, http://dx.doi.org/10.1016/j.tcb.2008.07.007.
[29] B.J. Reinhart, F.J. Slack, M. Basson, A.E. Pasquinelli, J.C. Bettinger, A.E. Rougvie, H.R. Horvitz, G. Ruvkun, The 21-nucleotide *let-7* RNA regulates developmental timing in *Caenorhabditis elegans*, Nature 403 (2000) 901–906, http://dx.doi.org/10.1038/35002607.
[30] A. Esquela-Kerscher, F.J. Slack, Oncomirs — microRNAs with a role in cancer, Nat. Rev. Cancer 6 (2006) 259–269, http://dx.doi.org/10.1038/nrc1840.
[31] X.-B. Shi, C.G. Tepper, R.W. deVere White, Cancerous miRNAs and their regulation, Cell Cycle 7 (2008) 1529–1538, http://dx.doi.org/10.4161/cc.7.11.5977.
[32] M. Deng, H.-L. Tang, X.-H. Lu, M.-Y. Liu, X.-M. Lu, Y.-X. Gu, J.-F. Liu, Z.-M. He, miR-26a Suppresses Tumor Growth and Metastasis by Targeting FGF9 in Gastric Cancer, PLoS One 8 (2013) e72662, http://dx.doi.org/10.1371/journal.pone.0072662.
[33] J. Gao, L. Li, M. Wu, M. Liu, X. Xie, J. Guo, H. Tang, X. Xie, MiR-26a Inhibits Proliferation and Migration of Breast Cancer through Repression of MCL-1, PLoS One 8 (2013) e65138, http://dx.doi.org/10.1371/journal.pone.0065138.
[34] X. Dang, A. Ma, L. Yang, H. Hu, B. Zhu, D. Shang, T. Chen, Y. Luo, MicroRNA-26a regulates tumorigenic properties of *EZH2* in human lung carcinoma cells, Cancer Genet. 205 (2012) 113–123, http://dx.doi.org/10.1016/j.cancergen.2012.01.002.
[35] J. Li, Y. Wang, Y. Song, Z. Fu, W. Yu, miR-27a regulates cisplatin resistance and metastasis by targeting RKIP in human lung adenocarcinoma cells, Mol. Cancer 13 (2014) 193, http://dx.doi.org/10.1186/1476-4598-13-193.
[36] S.U. Mertens-Talcott, S. Chintharlapalli, X. Li, S. Safe, The Oncogenic microRNA-27a Targets Genes That Regulate Specificity Protein Transcription Factors and the G_2-M Checkpoint in MDA-MB-231 Breast Cancer Cells, Cancer Res. 67 (2007) 11001–11011, http://dx.doi.org/10.1158/0008-5472.CAN-07-2416.
[37] R. Wahlroos, J. Toivonen, M. Tirri, P. Hänninen, Two-Photon Excited Fluorescence Energy Transfer: A Study Based on Oligonucleotide Rulers, J. Fluoresc. 16 (2006) 379–386, http://dx.doi.org/10.1007/s10895-006-0084-x.
[38] M. Massey, W.R. Algar, U.J. Krull, Fluorescence resonance energy transfer (FRET) for DNA biosensors: FRET pairs and Förster distances for various dye–DNA conjugates, Anal. Chim. Acta 568 (2006) 181–189, http://dx.doi.org/10.1016/j.aca.2005.12.050.
[39] Y. Yang, J. Huang, X. Yang, K. Quan, H. Wang, L. Ying, N. Xie, M. Ou, K. Wang, FRET Nanoflares for Intracellular mRNA Detection: Avoiding False Positive Signals and Minimizing Effects of System Fluctuations, J. Am. Chem. Soc. 137 (2015), http://dx.doi.org/10.1021/jacs.5b04007.
[40] H.-N. Wang, A.M. Fales, T. Vo-Dinh, Plasmonics-based SERS nanobiosensor for homogeneous nucleic acid detection, Nanomed. Nanotechnol. Biol. Med. 11 (2015) 811–814, http://dx.doi.org/10.1016/j.nano.2014.12.012.
[41] N.R. Markham, M. Zuker, DINAMelt web server for nucleic acid melting prediction, Nucleic Acids Res. 33 (2005) W577–W581, http://dx.doi.org/10.1093/nar/gki591.
[42] N.R. Markham, M. Zuker, UNAFold, in: J.M. Keith (Ed.), Bioinformatics, Humana Press, Totowa, NJ, 2008, pp. 3–31. http://www.springerprotocols.com/Abstract/doi/10.1007/978-1-60327-429-6_1 (accessed July 22 2015).
[43] DINAMelt | mfold.rit.albany.edu, (n.d.). http://mfold.rna.albany.edu/?q=DINAMelt (accessed July 22 2015).
[44] L. Wang, C.J. Yang, C.D. Medley, S.A. Benner, W. Tan, Locked nucleic acid molecular beacons, J. Am. Chem. Soc. 127 (2005) 15664–15665, http://dx.doi.org/10.1021/ja052498g.
[45] K. Martinez, M.-C. Estevez, Y. Wu, J.A. Phillips, C.D. Medley, W. Tan, Locked nucleic acid based beacons for surface interaction studies and biosensor development, Anal. Chem. 81 (2009) 3448–3454, http://dx.doi.org/10.1021/ac8027239.
[46] S.A. Melo, R. Kalluri, miR-29b moulds the tumour microenvironment to repress metastasis, Nat. Cell Biol. 15 (2013) 139–140, http://dx.doi.org/10.1038/ncb2684.
[47] A. Fegan, P.S. Shirude, S. Balasubramanian, Rigid cyanine dye nucleic acid labels, Chem. Commun. (2008) 2004–2006, http://dx.doi.org/10.1039/b801629a.